

Article

Synthesis and Characterization of Sustainable Eco-Friendly Alkali-Activated High-Content Iron Ore Tailing Bricks

Xiangyang Kang¹, Yanman Li¹, Wei Li¹, Yuxian Zhou¹, Jiarui Cui¹, Baohua Cai¹, Yong Zi¹, Jing Fang¹, Yongqing Chen², Senlin Li^{3,4,5,*}  and Xin Kang^{3,4,5,*}

- ¹ China Nuclear Dadi Exploration and Technical Design Co., Ltd., Beijing 100013, China; kangxiangyang@cnuc.cn (X.K.); liyanman@cnuc.cn (Y.L.); liwei@cnuc.cn (W.L.); zhouyuxian@cnuc.cn (Y.Z.); gky240@cnuc.cn (J.C.); caibaohua@cnuc.cn (B.C.); ziyong@cnuc.cn (Y.Z.); fangjing@cnuc.cn (J.F.)
- ² School of Transportation Engineering, East China Jiaotong University, Nanchang 330013, China; 3473@ecjtu.edu.cn
- ³ Key Laboratory of Building Safety and Energy Efficiency of the Ministry of Education, Hunan University, Changsha 410082, China
- ⁴ National Center for International Research Collaboration in Building Safety and Environment, Hunan University, Changsha 410082, China
- ⁵ College of Civil Engineering, Hunan University, Changsha 410082, China
- * Correspondence: lisenlin@hnu.edu.cn (S.L.); kangxin@hnu.edu.cn (X.K.)

Abstract: With the development of urbanization, the demand for bricks continues to increase. However, traditional brick production methods result in significant energy consumption and environmental pollution. In Hebei Province, China, historical mineral extraction activities have left behind substantial iron ore tailings (IOT). With the objective of recycling IOT resources and promoting ecological restoration and sustainable development, the feasibility of producing alkali-activated bricks using iron ore tailings was explored. This study primarily utilized IOT supplemented with ground granulated blast-furnace slag (GGBS) to successfully synthesize sustainable eco-friendly alkali-activated high-content IOT bricks. Experimental investigations were conducted to explore the effects of the raw material mixing ratio, content, and modulus of the alkaline activator, molding pressure, and grain size distribution on the strength. The research demonstrated that the IOT: GGBS ratio of 85:15 met the requirements of the Chinese JC/T422-2007 MU25 standard, resulting in compressive and flexural strengths of 31.72 MPa and 2.83 MPa, respectively. Increasing the alkali activator content enhanced the brick strength, with an optimal alkali activator modulus of 1 M. Moreover, the molding pressure significantly improved brick strength and also enhanced the particle-to-particle contact density. Bricks prepared using finer particle size IOT exhibited higher compressive strength, whereas flexural strength remained relatively unaffected by particle size distribution. Furthermore, a comprehensive analysis of the microstructure and alkali activation mechanism of IOT-GGBS bricks was performed using XRD, SEM, FTIR, and AFM techniques. The results indicated that IOT primarily acted as an aggregate and partially participated in the reaction, whereas GGBS reacted extensively, generating C-S-H gel and C-A-H, providing robust bonding strength. Additionally, the increase in GGBS content led to the partial disintegration of some IOT particles, forming more stable aggregates under the influence of the C-S-H gel. This study offers theoretical guidance for the efficient utilization of IOT in construction materials, thereby contributing to the promotion of sustainable development and environmental conservation.

Keywords: alkali activation; compressive strength; flexural strength; GGBS; IOT; microstructure



Citation: Kang, X.; Li, Y.; Li, W.; Zhou, Y.; Cui, J.; Cai, B.; Zi, Y.; Fang, J.; Chen, Y.; Li, S.; et al. Synthesis and Characterization of Sustainable Eco-Friendly Alkali-Activated High-Content Iron Ore Tailing Bricks. *Buildings* **2023**, *13*, 2743. <https://doi.org/10.3390/buildings13112743>

Academic Editor: Ana Luísa Velosa

Received: 22 September 2023

Revised: 20 October 2023

Accepted: 26 October 2023

Published: 30 October 2023



Copyright: © 2023 by the authors. Licensee MDPI, Basel, Switzerland. This article is an open access article distributed under the terms and conditions of the Creative Commons Attribution (CC BY) license (<https://creativecommons.org/licenses/by/4.0/>).

1. Introduction

The ongoing growth in urban housing and infrastructure projects has led to an ever-increasing demand for construction materials in civil engineering. This surge in demand specifically pertains to bricks [1–3]. Traditional brick manufacturing processes involve

preparing raw materials, typically a mixture of sand, clay, and shale, followed by firing them in high-temperature kilns [4–6]. However, these conventional firing techniques incur substantial energy consumption and greenhouse gas emissions during production, resulting in severe environmental pollution [7]. Moreover, the substantial clay consumption for brick production, particularly on agricultural land, has inflicted considerable damage on land resources [8,9]. To safeguard the ecological environment and promote sustainability, it is imperative to develop alternative brick-making materials for the production of sustainable and eco-friendly bricks, aiming to alleviate environmental pressures while fulfilling the requirements of the construction industry.

Tailings are solid waste generated inevitably during the mining process, contributing to air, soil, and groundwater pollution while also triggering geological hazards [10]. In China, the total production of tailings has surpassed 600 million tons, with iron ore tailings (IOT) accounting for approximately 40% of this total. However, the overall utilization rate of tailings remains below 20%, with IOT exhibiting a utilization rate of less than 7% [11–13]. The high iron ion content in IOT makes its accumulation prone to acid mine drainage [14,15], leading to water pollution, severe land degradation, and latent geological hazards [16]. In Huai'an County, Hebei Province, China, abundant iron ore resources exist, as shown in Figure 1. Nevertheless, historical mining activities have left nearly a hundred IOT reservoirs and substantial IOT deposits, exerting immense pressure on land resources and causing ecological deterioration. Currently, the comprehensive and efficient utilization of IOT represents a critical issue that local governments urgently need to address. On one hand, this is in pursuit of recycling IOT and facilitating ecological restoration. On the other hand, it aims to meet the increasing demand for construction materials while driving economic development in resource-depleted regions. Therefore, it is imperative to make full use of IOT and implement eco-friendly brick production.

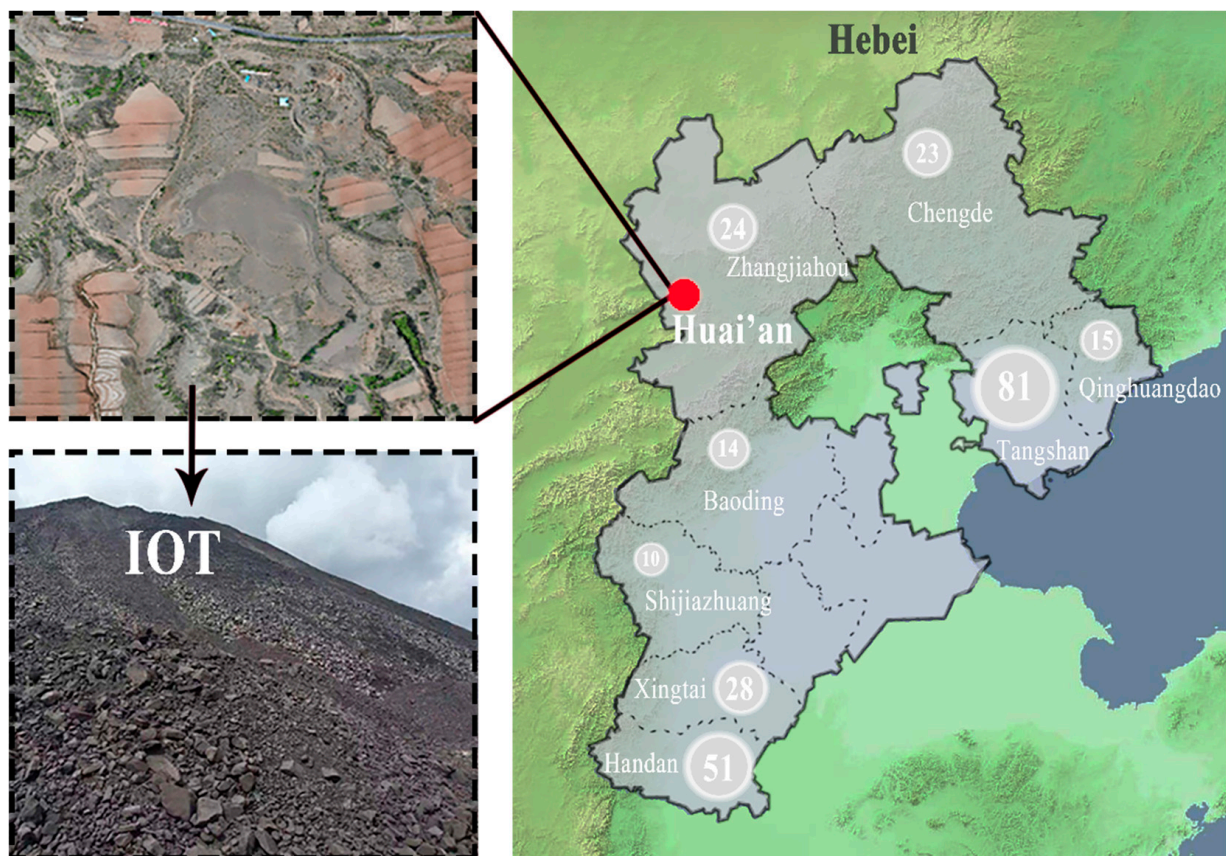


Figure 1. The number of iron ore mines in Hebei and the iron ore mine in Huai'an.

In fact, IOT is a type of fine-grained solid waste rich in SiO_2 and Al_2O_3 , with the potential for pozzolanic activity [17,18]. Utilizing IOT as a mineral admixture in the production of construction materials, such as bricks [19], cement [20,21], and concrete [22,23], is considered a viable approach that contributes to waste utilization and sustainable development. Currently, numerous studies have examined the feasibility and methods of producing bricks from IOT. Fontes et al. [24] demonstrated that increasing the bulk density of IOT and adjusting the water content could enhance the mechanical properties of IOT bricks. Mendes et al. [25] investigated the feasibility of preparing sintered bricks from a mixture of low-dose IOT and clay, with optimal results achieved at a mass ratio of 29.1% for IOT, meeting international standards. Chen et al. [26] utilized a mixture with a mass ratio of 84:10:6 for IOT, clay, and fly ash, employing a process involving mixing, forming, drying, and firing to produce high-content sintered bricks, effectively utilizing IOT. Yang et al. [27] added fly ash to low-silicon IOT and produced sintered bricks at temperatures between 900 and 1000 °C. Mechanical tests showed that these bricks could serve as substitutes for traditional clay or shale-based bricks. Luo et al. [28] employed a blend of IOT and coal gangue powder as primary materials and shale and sludge as binders to successfully produce composite sintered bricks. The study revealed that with increasing sintering temperature, pseudo-crystalline mineral particles significantly increased, accompanied by the appearance of glassy liquid phase inclusions and fine-grained pseudo-crystalline mineral particles, resulting in a more uniform and denser surface. Zhao et al. [29] used a mixture of 70% IOT, 15% lime, and 15% sand to produce steam-pressed bricks, investigating the hydration process of the IOT-lime-sand system. Analysis via XRD, DSC, IR, and SEM revealed that tobermorite played a pivotal role in determining the strength of the steam-pressed bricks. Liu et al. [30] demonstrated that under the influence of alkali activators, IOT could increase specific surface area, enhance surface energy, and promote the formation of a significant amount of needle-like ettringite (AFt) and calcium silicate hydrate (C-S-H) gel, leading to a denser microstructure. H.K. and Hossiney [31] successfully produced alkali-activated bricks using fly ash, GGBS, and IOT as the raw materials. However, it is worth noting that the utilization of IOT in alkali-activated bricks could meet the construction standards only when the IOT content was below 50%. In summary, previous research clearly demonstrated the feasibility of using IOT for brick production. However, most high-content IOT bricks are either traditional sintered or steam-pressed bricks, whereas the utilization of IOT in low-energy and low-pollution alkali-activated bricks remains relatively low.

Granulated blast-furnace Slag (GGBS) is solid waste generated during the iron smelting process. Due to its small particle size, large specific surface area, and relatively high glassy phase content, GGBS possesses significant potential reactivity and is widely used as an alkali activator precursor [32]. Gokul et al. [33] achieved favorable results by enhancing the stability of clay through the addition of GGBS in an alkali-activated reaction. When the GGBS content reached 24%, the unconfined compressive strength of the clay after 28 days reached 4.06 MPa. Liu et al. [34] designed and proposed GGBS-based high-volume converter steel slag composite carbonation curing mortar. FTIR analysis indicated that the main reaction products after the composite activation were calcium carbonate and CASH gel. Alam et al. [35] investigated the impact of different GGBS contents on the strength of red mud and found that the best alkali activation results were achieved with 25% GGBS and 1M sodium silicate, significantly improving the compressive and impact strengths of the red mud. These findings illustrated that GGBS, as an alkali activator precursor, could effectively participate in the reuse of solid waste in construction materials. Therefore, the aim of this study was to incorporate GGBS into IOT to enhance the alkali activation reactivity and promote the production of high-content IOT alkali-activated bricks.

In this study, IOT served as the primary raw material and was activated using a sodium silicate solution, with the addition of GGBS as a precursor, to manufacture sustainable and environmentally friendly bricks. A series of experiments were conducted to investigate the effects of the raw material mixing ratio, content, and modulus of the alkaline activator, molding pressure, and grain size distribution on the strength of the bricks. Additionally, the

microstructure and mechanical properties of the materials were comprehensively examined via XRD, SEM, FTIR, and AFM analyses. This paper provides theoretical guidance for the efficient utilization of IOT in the production of construction materials, contributing to the advancement of solid waste utilization and the alleviation of environmental pressures.

2. Materials and Methods

2.1. Materials

IOTs were obtained from a mining site in Huai'an, Hebei Province. The grain size distribution and specific surface area of the raw material were determined using a Chinese BT-9300HT laser grain size analyzer, as shown in Figure 2. The grain sizes were mainly distributed in the range of 100–500 μm , with an average grain size of 207.20 μm . Additionally, the average specific surface area of IOT particles was measured to be 20.52 m^2/kg . X-ray fluorescence (XRF) analysis was employed to determine the chemical composition of the material, and the results are presented in Table 1, with SiO_2 , Al_2O_3 , and CaO content of 54.41%, 13.84%, and 8.30%, respectively. Notably, the content of Fe_2O_3 was found to be 13.01%. Figure 3 shows the XRD image of IOT, indicating the main mineral components of IOT include Hematite (Fe_2O_3), Enstatite [$(\text{Mg}, \text{Ca}, \text{Fe}, \text{Al})\text{Si}_2\text{O}_6$], and Quartz (SiO_2). Due to its high Enstatite content, IOT can provide alkali metal ions with large ionic radii, such as Mg^{2+} , Ca^{2+} , and Fe^{3+} . These alkali metal ions can induce distortions in the aluminosilicate glass, disrupting the weaker $-\text{O}-\text{Al}-\text{O}-$ bonds and increasing non-bridging oxygen sites, thereby reducing the polymerization degree [36–38]. Figure 4a depicts the microscopic morphology of IOT, which exhibits a rough, irregular, and fragmented surface that forms larger pores upon accumulation.

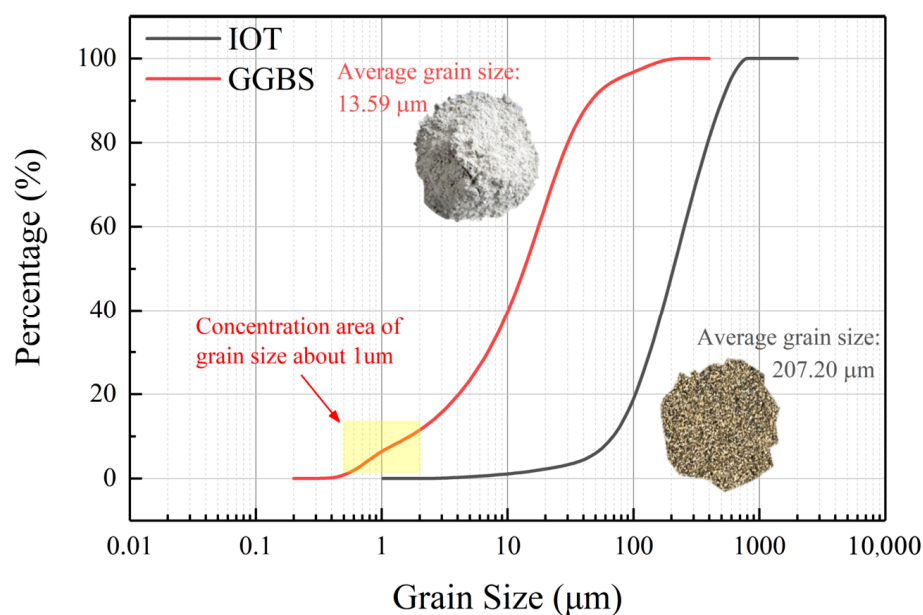


Figure 2. The grain size distribution of IOT and GGBS.

Table 1. Chemical composition of IOT and GGBS (wt%).

Chemical Composition	SiO_2	Al_2O_3	Fe_2O_3	CaO	MgO	Others
IOT	54.41	13.84	13.01	8.30	4.63	5.81
GGBS	34.50	17.70	1.03	34.00	6.01	6.76

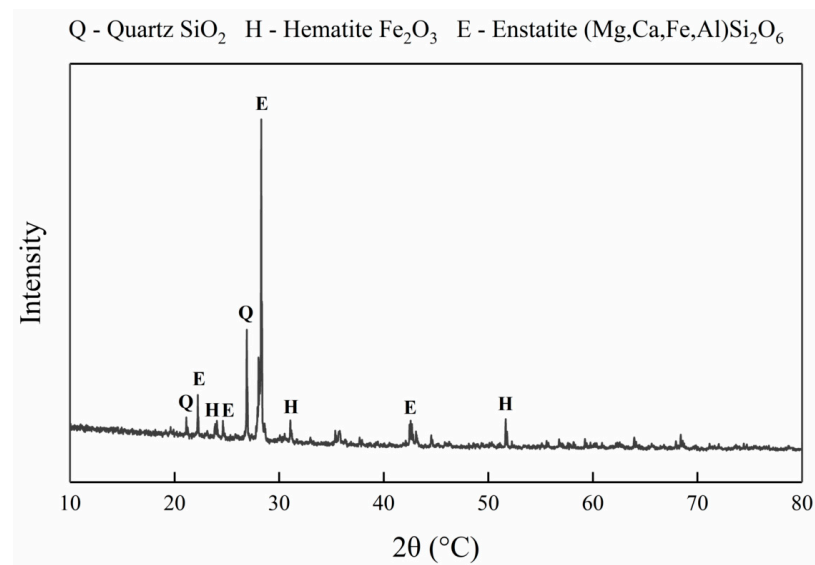


Figure 3. XRD image of the raw material IOT.

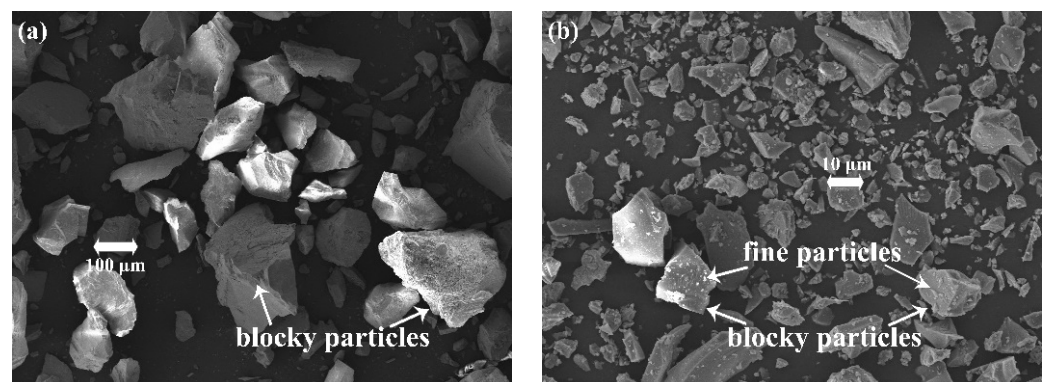


Figure 4. The SEM images of: (a) IOT; (b) GGBS.

GGBS was procured from a material company in Gongyi, Hebei Province. As shown in Figure 2, the grain size distribution of GGBS primarily fell within the range of 1–35 μm , with an average grain size of 13.59 μm , which was one order of magnitude smaller than that of the IOT. Notably, there was a small grain size distribution of around 1 μm , accounting for approximately 10% of the total. GGBS exhibited an average specific surface area of 491 m^2/kg , which was 20 times greater than that of IOT, indicating a propensity for the alkali activation reaction. The major chemical components of GGBS are presented in Table 1, with SiO_2 , Al_2O_3 , and CaO contents at 34.50%, 17.70%, and 34.00%, respectively. Figure 4b depicts the microscopic morphology of GGBS, which is characterized by irregular blocky particles with a minor amount of fine particles adhering to the surface.

In this study, liquid sodium silicate was employed as an alkali activator. The product was procured from a material company located in Wuxi City, Jiangsu Province. The liquid sodium silicate had a modulus of 2.31, with a 42% content of Na_2O , which was adjusted by the addition of Na_2O to achieve the desired modulus.

2.2. Sample Preparation

To cater to the specific objectives of different experiments, various experimental variables were defined. These variables encompassed the raw material mixing ratio (IOT to GGBS), content and modulus of the alkaline activator, molding pressure, and grain size distribution of IOT (Table 2). Typically, these parameters were employed during the preparation process using the values or ratios provided in Table 3.

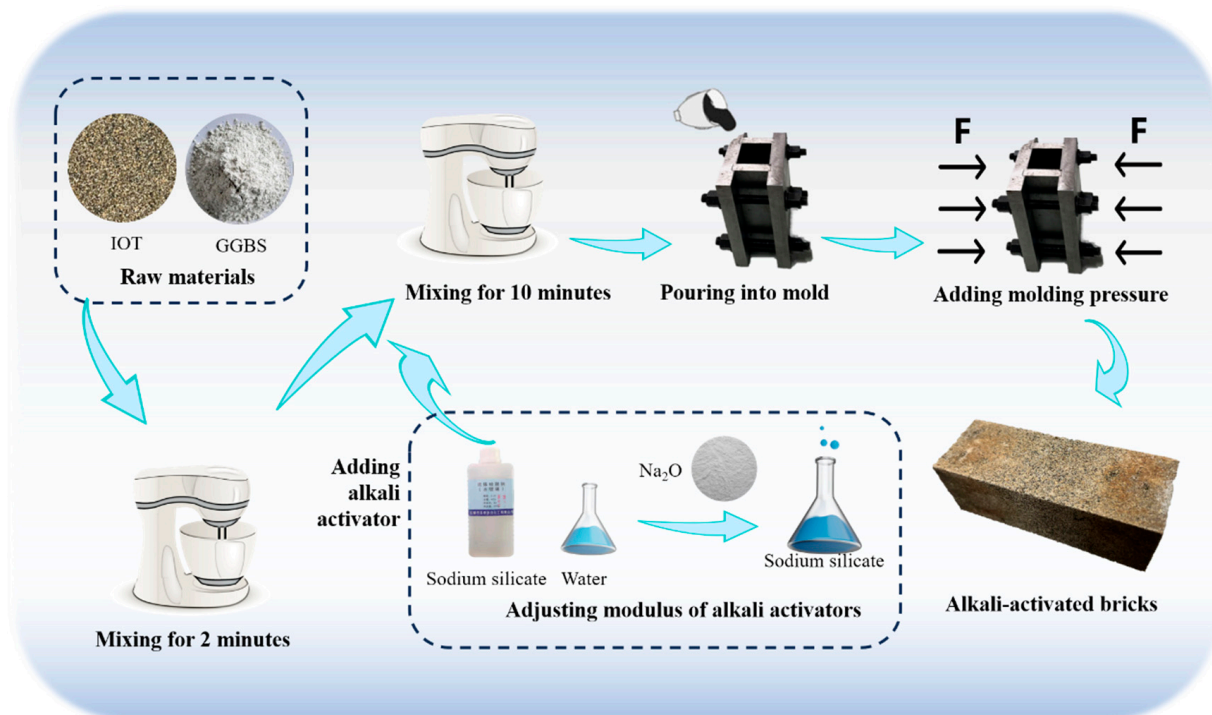
Table 2. The grain size ratio of different types of IOT.

	Grain Size Interval (%)			IOT Type
	<0.25 mm	0.25–0.4 mm	>0.4 mm	
Ratio	2	3	5	A
	3	3	4	B
	4	3	3	C
	6	2	2	O
	(59.31)	(21.85)	(18.84)	

Table 3. Default parameters in sample preparation.

Parameter	Raw Materials Ratio	Content of Alkali Activator	Modulus of Alkali Activator	Molding Pressure	Grain Size Ratio
Value/Ratio	90:10	15%	1.5 M	20 MPa	59.31:21.85:18.84

The procedural workflow of the sample preparation is outlined below, and it is referenced in Figure 5.

**Figure 5.** The flowchart of the process of producing alkali-activated IOT brick.

The sample preparation process was as follows: First, IOT and GGBS were thoroughly mixed in a mixer at different mass ratios for 2 min. Next, a specific amount of sodium silicate with Na₂O was mixed to adjust the modulus of the alkali activator, and then the alkali activator was slowly added to the mixtures by stirring for 10 min to ensure a complete reaction. The mixtures were poured into a rectangular mold (40 × 40 × 180 mm) after thorough mixing, compacted under different molding pressures, and demolded after 30 min and 1 day, depending on the modulus. Finally, the samples were cured for 7 days at room temperature.

2.3. Test Methods

Considering different raw material mixing ratios, alkali activator contents and modulus, molding pressures, and grain size distribution, the mechanical performance indicators

of alkali-activated bricks, such as unconfined compressive strength and flexural strength, were determined according to the Chinese JC/T422-2007 standard.

The chemical compositions of the samples were analyzed using Axios PANalytical Axios X-ray fluorescence (XRF) spectrometry with Rhodium (Rh) as the target material. The mineral compositions of the samples were determined using a Rigaku SmartLab SE X-ray diffraction (XRD) instrument with Cu-K α radiation in the scanning range of 10° to 80° and a scanning speed of 10°/min. The XRD test results were analyzed using the HighScore Plus 3.05 software. The microstructure and morphology of the samples were observed using a TESCAN MIRALMS scanning electron microscope (SEM). Furthermore, the FTIR spectra of the samples were obtained using a Bruker Vertex 70 infrared spectrometer, with a wavelength ranging from 400 to 4000 cm⁻¹. The microscale mechanical properties and microstructures were characterized using a Park XE7-type Atomic Force Microscope (AFM). The block sample was fixed in the resin material, ground into a plane, and polished. Then, the samples were analyzed using the AC160TS cantilever in in F/D mode after the scanning area was divided into 8 × 8 unit cells. And the XEI 4.3.4 software was used to calculate the micromechanical stiffness of the alkali-activated IOT-GGBS bricks.

3. Results and Discussion

3.1. Effect of the Raw Material Mixing Ratio on the Brick Properties

Compared to the higher alkali activation of GGBS [33], the lower alkali activation of IOT significantly affected the mechanical performance of alkali-activated bricks [39], especially concerning the raw material mixing ratio. An IOT content exceeding 80% was required to prepare high-dosage IOT bricks. In order to determine the ideal raw material mixing ratio that met the requirements for high-strength and high-content bricks, samples were prepared in three different proportions: IOT:GGBS = 80:20, 85:15, and 90:10, under other conditions as outlined in Table 3.

The results of the mechanical performance test of the bricks are presented in Figure 6, where the black dashed line represents the compressive strength of the JC/T422-2007 MU25, and the red line represents the flexural strength. The results indicate that both the compressive and flexural strengths of the bricks significantly decreased as the IOT content increased (or GGBS content decreased). The compressive strength dropped by half from 61.55 MPa at 80% IOT content to 31.72 MPa at 85% IOT content and continued to decline to 14.05 MPa at 90% IOT content, where the compressive strength no longer met the MU25 standard. Similarly, the flexural strength gradually decreased from 6.86 MPa at 80% IOT content to 1.23 MPa at 90% IOT content, and at 90% IOT content the flexural strength also failed to meet the MU25 standard. The reason for the strength reduction was the decrease in the content of GGBS, which had stronger alkaline activity. Almost all GGBS particles had smaller grain sizes than the IOT particles (Figure 1). Therefore, with less GGBS content, there was a lower amount of C-S-H gel generated via the alkali-activated reaction covering the surface of IOT particles and filling the pores [40]. Consequently, the tight bonding between IOT particles was weakened. Furthermore, when the IOT content was too high, the overall alkali activity of the samples decreased, resulting in a lower degree of alkali-activated reaction. Based on the test results, the optimal raw material mixing ratio to meet the MU25 standard for high-strength and high-content IOT bricks was IOT:GGBS = 85:15.

3.2. Effect of the Content and Modulus of Alkaline Activator on the Brick Properties

Alkali activators played a significant catalytic role in the reaction process, and their content and modulus affected the preparation time and strength of alkali-activated bricks. According to previous studies, a higher content of alkali activator was required when preparing alkali-activated materials using IOT or similar minerals [41,42]. Therefore, the test included varying alkali activator contents of 10%, 15%, and 20%, and test moduli of 1, 1.5, and 2 M. The results of the mechanical performance tests are presented in Figures 7 and 8.

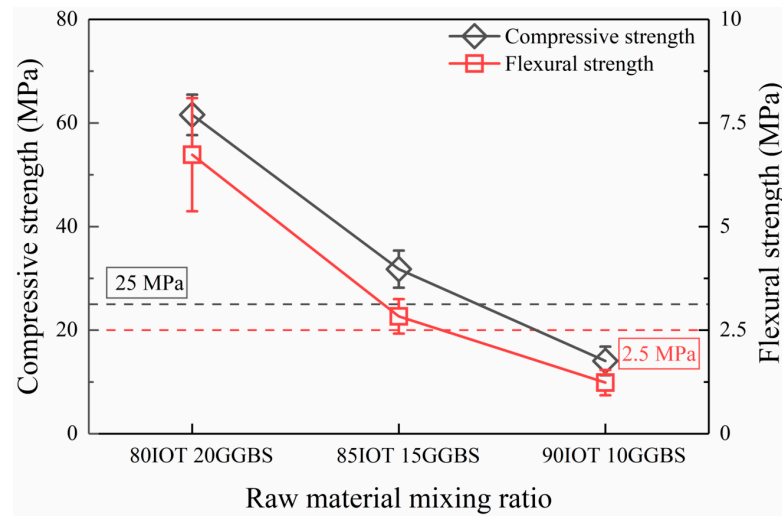


Figure 6. The compressive strength and flexural strength of bricks with different mixing ratios.

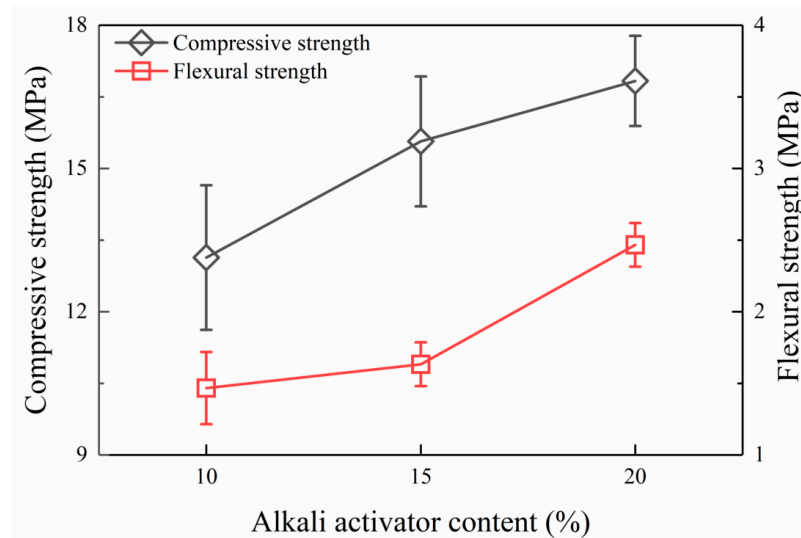


Figure 7. The compressive strength and flexural strength of bricks with different alkali activator contents.

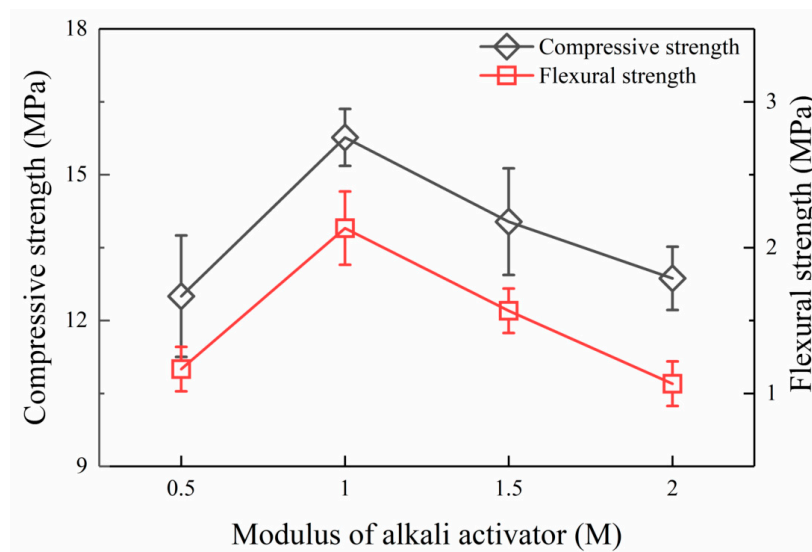


Figure 8. The compressive strength and flexural strength of bricks with different moduli of alkali activator.

The results show that increasing the content of the alkali activator effectively enhanced the compressive and flexural strength of the bricks (Figure 7). At an alkali activator content of 10%, the compressive strength was 13.12 MPa. When the content increased to 15% and 20%, the compressive strength rose to 15.58 MPa and 16.83 MPa, representing increases of 19% and 28%, respectively. Similarly, the flexural strength increased with a higher content of alkali activator, increasing from 1.48 MPa to 1.64 MPa and 2.46 MPa, indicating that the flexural strength was increased about 11% and 68%, respectively. This is because a higher content of alkali activator could more effectively dissolve the silicon-aluminum components in IOT and GGBS, exhibiting a faster reaction rate. This rapidly formed a C-S-H gel, which bonded both unreacted solid particles and partially dissolved solids more tightly [43]. As a result, interparticle bonding became more compact, leading to improved mechanical properties, especially a significant increase in flexural strength.

Figure 8 illustrates that both the compressive and flexural strengths initially increased and then decreased with the modulus of the alkali activator. The maximum strength occurred at a modulus of 1 M, reaching 16.10 MPa and 2.13 MPa, respectively, which aligned with previous research [44,45]. This suggested that both excessively low and high moduli of the alkali activators might decrease the mechanical performance of the bricks. When the modulus was too low, such as 0.5 M, the alkali activator provided an insufficient amount of soluble silica, resulting in fewer nucleation sites [46]. This made it challenging for Si to undergo an aggregation reaction with Ca^{2+} and Al^{3+} in the liquid phase, consequently leading to lower compressive and flexural strength [43]. As the modulus increased to 1 M, the quantity of soluble silica increased, along with the corresponding nucleation sites, which promoted the reaction process and maximized the strength of the bricks. However, when the modulus of the alkali activator reached 1.5 M and 2 M, the silicon released from the sodium silicate solution, IOT, and GGBS became oversaturated, leading to the formation of a significant amount of C-S-H gel covering the precursors. Alternatively, it might precipitate as zeolite crystals in the form of silicate tetrahedra, hindering further reaction progress and causing a reduction in strength [47].

3.3. Effect of the Molding Pressure on the Brick Properties

The molding pressure directly affected the degree of contact degree between the material particles and the alkali-activating solution, thereby influencing the compactness of the bricks. The mechanical performance test results of the alkali-activated bricks prepared at molding pressures of 20, 40, and 60 MPa are shown in Figure 9.

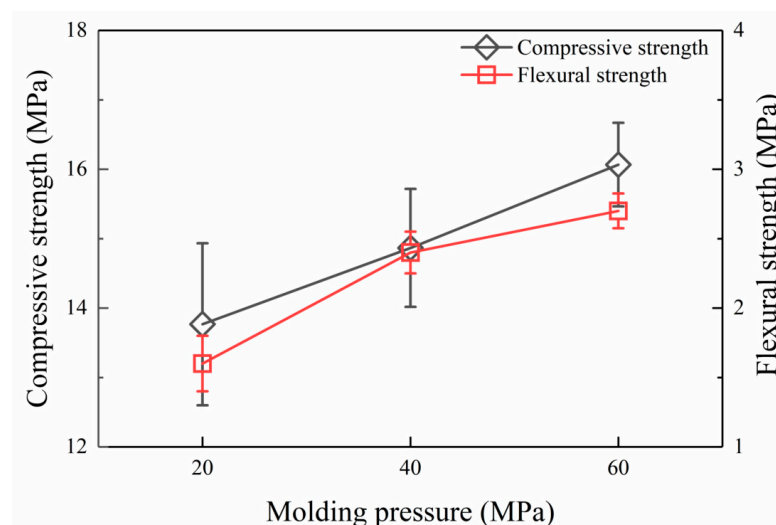


Figure 9. The compressive strength and flexural strength of bricks under different molding pressures.

Both the compressive strength and the flexural strength of the bricks increased with increasing molding pressure. In particular, at molding pressures of 20, 40, and 60 MPa, the

compressive strengths were 13.75 MPa, 14.86 MPa, and 16.02 MPa, respectively, whereas the flexural strengths were 1.61 MPa, 2.39 MPa, and 2.72 MPa, respectively. Additionally, the error bars in the statistical results of the test data became smaller with increasing molding pressure, indicating that bricks prepared under higher molding pressures had a more uniform internal structure and more stable mechanical performance. Prasanphan et al. [48] suggested that additional pressure during the alkali-activation reaction allows the release of air trapped between raw material pores, increasing the contact area between the alkaline solution and reactants. At higher molding pressures, the air trapped within the pores was further expelled, and smaller-sized GGBS particles tended to fill the gaps between larger-sized IOT particles. Consequently, particle aggregation became easier, enhancing structural compactness. The surfaces of the formed compact aggregates dissolved layer by layer in an alkaline environment, generating C-S-H gel, which positively affected the strength of the bricks [49]. Therefore, with increasing molding pressure, the contact between particles became tighter, resulting in stronger internal bonding and cohesion within the bricks, ultimately leading to a higher compressive strength.

3.4. Effect of the Grain Size Gradation of IOT on the Brick Properties

In order to investigate the contribution of IOT grain size to the performance of alkali-activated bricks, bricks were prepared by proportionally mixing IOT particles of different sizes and were subjected to performance testing. IOT particles from different size intervals were mixed in accordance with the proportions specified in Table 2 to form three types of IOT particles, denoted as A, B, and C, where “O” represents the original IOT particles. The mechanical performance test results of the alkali-activated bricks with different particle sizes are presented in Figure 10.

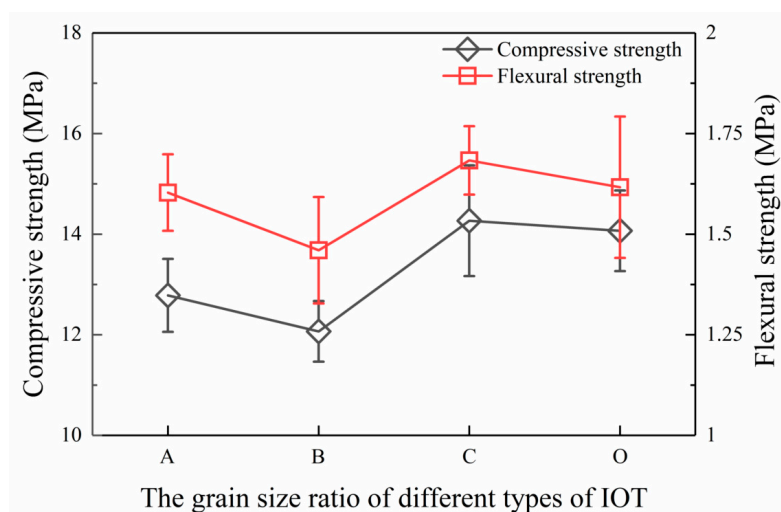


Figure 10. The compressive strength and flexural strength of bricks with different grain size ratios of IOT.

Figure 10 illustrates that B bricks exhibited the lowest strength, with compressive and flexural strengths of 11.85 MPa and 1.46 MPa, respectively. The C bricks, on the other hand, displayed the highest strength, with compressive and flexural strengths of 14.35 MPa and 1.72 MPa, respectively. The A bricks demonstrated strength levels similar to those of the B bricks, whereas the O bricks closely resembled the C bricks in terms of strength. According to Table 2, Type A IOT had the highest proportion of large-sized particles, whereas Type O IOT had the lowest proportion of small-sized particles. The particle distribution in the IOT, from Type A to Type O, transitioned from being predominantly composed of large-sized particles (>0.4 mm) to predominantly small-sized particles (<0.25 mm). It could clearly be seen that alkali-activated bricks made primarily from small-sized particles of IOT tended to exhibit higher compressive strength, whereas those dominated by large-sized particles

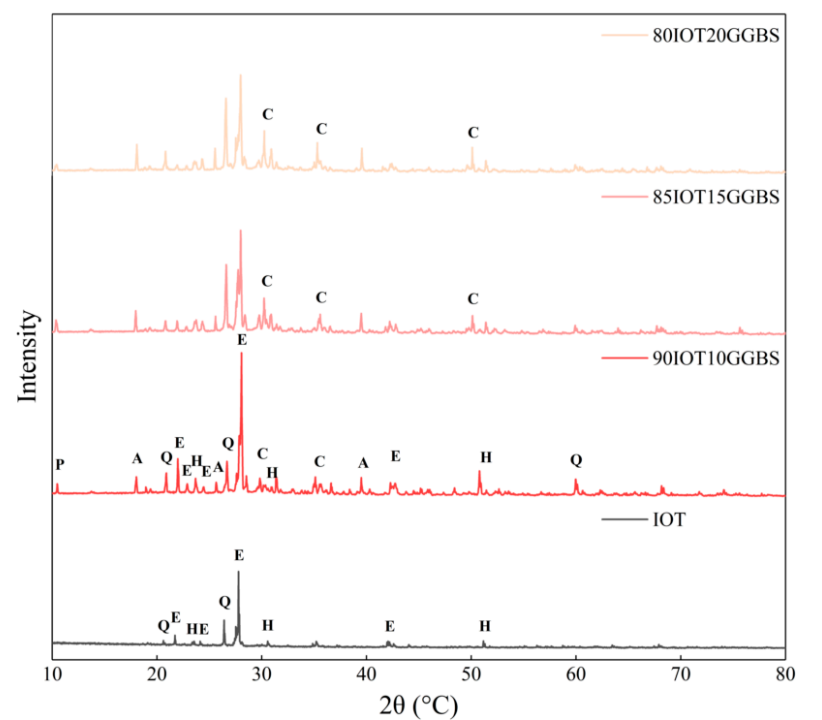
displayed lower strength. This phenomenon might be attributed to the fact that small-sized IOT particles not only filled or covered the pores of larger IOT particles but were also filled or covered by smaller-sized GGBS particles [50,51], facilitating the production of hydration products and interparticle bonding. It is worth noting that when an excessive amount of small-sized IOT particles was present, the compressive strength of the bricks slightly decreased. This occurred because an excess of small-sized particles led to the creation of pores that GGBS particles could not adequately fill or cover.

Although the flexural strength exhibited a similar trend to the compressive strength, the change was minimal, with fluctuations not exceeding 0.25 MPa. The flexural strength of the bricks primarily depended on the tight bonding between the particles induced by the C-S-H gel formed during the alkali-activated reaction [52,53], rather than the grain size distribution.

3.5. Microstructure of the Specimens

3.5.1. XRD Analysis

The XRD patterns of IOT and alkali-activated IOT-GGBS bricks are presented in Figure 11. The XRD patterns of the IOT-GGBS bricks reveal that the primary products of the alkali-activated reaction were C-S-H gel (calcium silicate hydrate, $\text{Ca}_5\text{H}_2\text{O}_{18}\text{Si}_6$) and C-A-H (Calcium Aluminum Oxide Hydrate, $\text{Ca}_3\text{Al}_2\text{O}_6\text{XH}_2\text{O}$). Some diffraction peaks corresponded to Potassicsadanagaite, Enstatite, and Quartz.



Q - Quartz SiO_2 H - Hematite Fe_2O_3 E - Enstatite $(\text{Mg,Ca,Fe,Al})\text{Si}_2\text{O}_6$ C - CSH $\text{Ca}_5\text{H}_2\text{O}_{18}\text{Si}_6$
 A - CAH $\text{Ca}_3\text{Al}_2\text{O}_6\text{XH}_2\text{O}$ P - Potassicsadanagaite $\text{K}_{0.75}\text{Na}_{0.25}\text{Ca}_2\text{Fe}^{2+}_3\text{Al}_{1.25}\text{Fe}^{3+}_{0.75}(\text{Si}_6\text{Al}_2\text{O}_{22})(\text{OH})_2$

Figure 11. XRD image of IOT and alkali-activated IOT-GGBS bricks.

For alkali-activated IOT-GGBS bricks with different mixing ratios, the intensities of the diffraction peaks for C-S-H and C-A-H gradually decreased as the IOT content increased, whereas the intensity of Enstatite's diffraction peak increased. This suggested that IOT only partially participated in the alkali-activated reaction, with GGBS serving as the primary reactant. Therefore, IOT primarily acted as aggregates, whereas GGBS played a pivotal role in forming C-S-H gel and providing bonding strength. This observation was consistent with the experimental results of the raw material mixing ratios in Section 3.1. Additionally, highly active GGBS was prone to forming a network structure with a higher polymerization

degree [54]. And the presence of the reaction product Potassicsadanagaite indicated the existence of a significant amount of free alkali metal ions in the alkali-activated bricks. The network structure of the glass was disrupted by these alkali metal ions and thus the production of low-polymerization C-S-H was accelerated.

3.5.2. SEM Analysis

SEM images (10 μm) of alkali-activated IOT-GGBS bricks with varying GGBS contents are shown in Figure 12. Overall, IOT particles with larger sizes exhibited lower degrees of reaction, with some of them being partially covered by C-S-H gel and a small amount of C-A-H. In contrast, GGBS, which had undergone a more extensive reaction, was enveloped by C-S-H gel, either on the surface of IOT or within its pores, forming bonds with IOT particles.

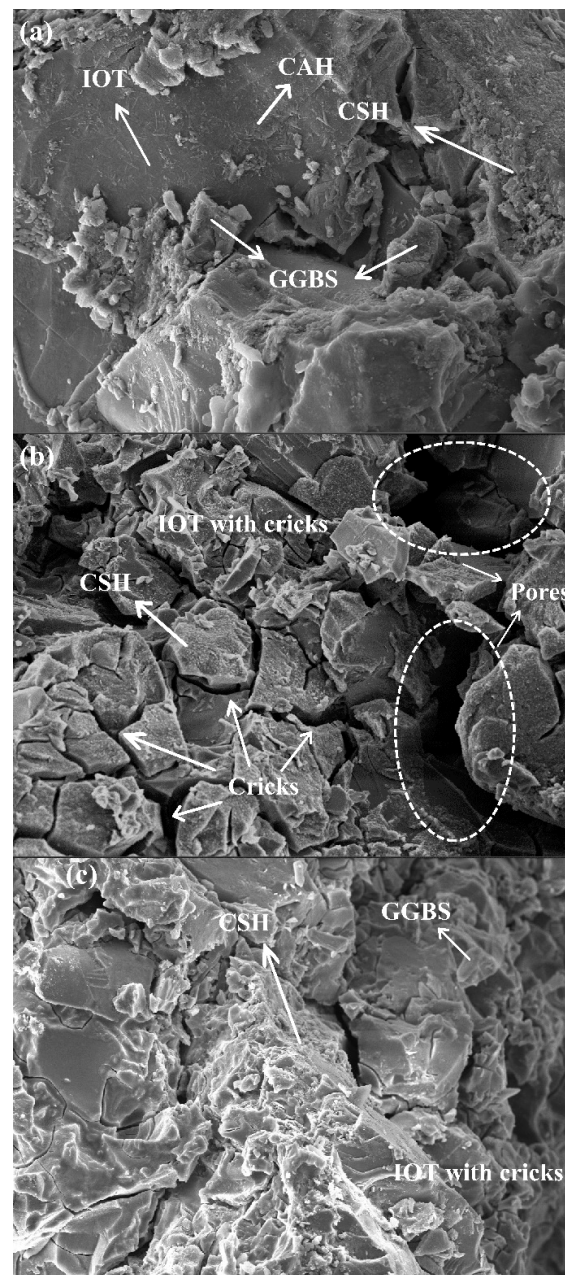


Figure 12. SEM images of alkali-activated IOT-GGBS bricks with (a) 10% content GGBS; (b) 15% content GGBS; (c) 20% GGBS content.

As the GGBS content increased, numerous cracks appeared on the surface of IOT particles (Figure 12b,c), accompanied by a greater coverage of the C-S-H gel. On the one hand, C-S-H gel appeared sporadically in a dot-like fashion on the fractured surfaces of IOT particles (Figure 12b), originating from the alkali-activated reaction of IOT itself. On the other hand, a significant amount of C-S-H gel bound multiple IOT fragments together (Figure 12c), which was attributed to the alkali-activated reaction of GGBS. This phenomenon might be attributed to the incorporation of GGBS, which not only increased the production of C-S-H gel but also heightened the overall alkali-activated activity of the reactants, consequently promoting the alkali-activated reaction of IOT (Section 3.2). Furthermore, the fragmentation of larger IOT particles into smaller ones facilitated further alkali-activated reactions, and GGBS, along with the C-S-H gel generated, infiltrated into the cracks, which contributed to the enhancement of compressive and flexural strengths.

3.5.3. FTIR Analysis

Figure 13 presents the FTIR spectra of IOT and alkali-activated IOT-GGBS bricks with varying GGBS contents. In the FTIR spectra of IOT, distinctive bands were observed at 468, 785, 1024, and 3440 cm^{-1} , corresponding to the in-plane bending vibrations of Si-O bonds, symmetric stretching vibrations of Si-O bonds, asymmetric stretching vibrations of Si-O/Al-O bonds, and stretching vibrations of $[\text{OH}]^-$, respectively [55–57]. At 1630 cm^{-1} , a weak band corresponding to the bending vibrations of H-O-H bonds was observed in the IOT spectrum [58]. In comparison, alkali-activated IOT-GGBS bricks exhibited a weak band at 876 cm^{-1} and a pronounced band at 1414 cm^{-1} , corresponding to the stretching vibrations of non-bridging oxygen in silicate tetrahedral structures and vibrations of Si-O bonds, respectively [59].

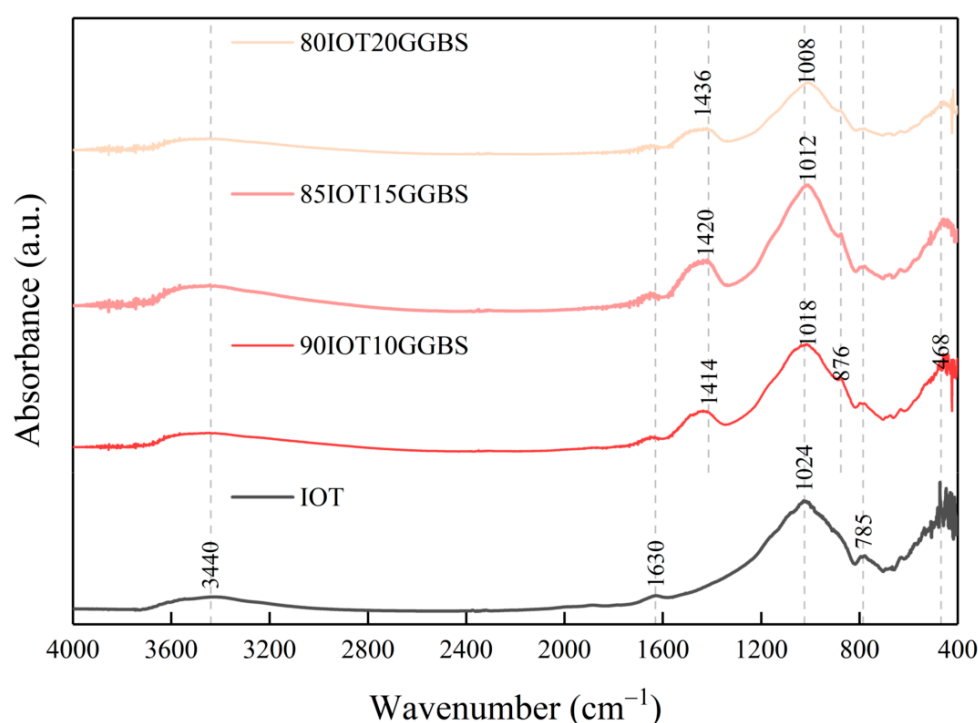


Figure 13. FTIR image of IOT and alkali-activated IOT-GGBS brick.

Both IOT and alkali-activated IOT-GGBS bricks shared absorption peaks around 468 and 785 cm^{-1} , 1630, and 3440 cm^{-1} , the former representing the bending and stretching vibrations of O-Si-O and Si-O-Si bonds, and the latter representing the bending and stretching vibrations of $[\text{OH}]^-$, which indicated the presence of hydroxyl groups or water in the C-S-H gel. For the alkali-activated IOT-GGBS bricks, the two characteristic bands at 876 and 1414 cm^{-1} confirmed the existence of low-polymerization C-S-H products. With an increase

in GGBS content, the wavenumbers of the asymmetric stretching vibrations of Si-O/Al-O bonds at 0%, 10%, 15%, and 20% GGBS content decreased from 1024 cm^{-1} to 1018 cm^{-1} , 1012 cm^{-1} , and 1008 cm^{-1} , indicating the depolymerization of more aluminosilicates in GGBS to form C-S-H gel and C-A-H [58]. Furthermore, the wavenumber of the Si-O bonds in low-polymerization C-S-H also increased with increasing GGBS content, suggesting that more GGBS contributed to the formation of low-polymerization C-S-H.

3.5.4. AFM Analysis

AFM morphology scanning ($10\text{ }\mu\text{m} \times 10\text{ }\mu\text{m}$) was conducted on alkali-activated IOT-GGBS bricks, and the microscale stiffness was calculated using XEI 4.3.4 software. The small scale of the probe led to variations in the measured microscale stiffness, resulting in relatively small numerical values. However, the trends remain convincing and representative. Figure 14a,b depict the 3D AFM morphology of IOT in alkali-activated IOT-GGBS bricks with 20% and 10% GGBS, along with the microscale stiffness matrix. For alkali-activated bricks containing 20% GGBS, although the surface of IOT particles (with an approximate grain size of $200\text{ }\mu\text{m}$) exhibited some undulations and a small amount of granular C-S-H, it appeared relatively smooth, lacking pronounced graininess. In contrast, in alkali-activated bricks with 10% GGBS content, the surface of the IOT particles was notably rough, with the presence of numerous C-S-H particles. This significant difference suggested that incorporating more GGBS into IOT as a precursor facilitated the progress of alkali activation reaction within the IOT-GGBS system. As a result, more C-S-H gels were generated, enveloping the IOT particles and leading to a smoother surface. Furthermore, the presence of unbound C-S-H particles (Figure 14b) on the surface of the IOT indicated that the alkali activation reaction on the IOT surface had a lower degree of progress.

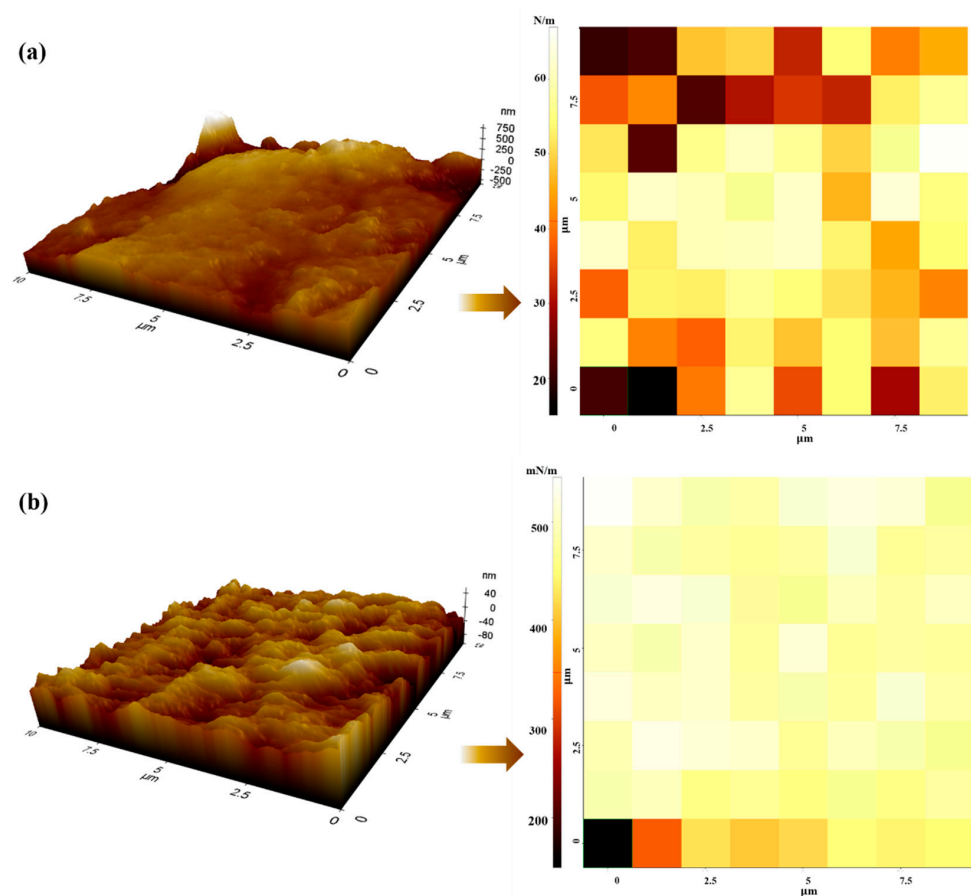


Figure 14. The AFM morphology images and stiffness matrix of IOI in (a) 80IOT20GGBS and (b) 90IOT10GGBS.

When the GGBS content was 20%, the average microscale stiffness calculated from the microscale stiffness matrix of the alkali-activated bricks was 43.27 N/m. The result was in close proximity to the AFM test results for alkali-activated geopolymers [51]. However, when the GGBS content was reduced to 10%, the average microscale stiffness of the alkali-activated bricks was 470.86 mN/m. These two values exhibited significant differences. The noticeable trend of decreasing stiffness with decreasing GGBS content indicated a reduced capacity of the material to resist deformation. This observation was consistent with the substantial differences in compressive strength discussed in Section 3.1.

3.6. Reaction Mechanism of Alkali-Activated IOT-GGBS Mixtures

Based on the analysis results from XRD, SEM, FTIR, and AFM, the reaction mechanism of the IOT-GGBS mixtures is illustrated in Figure 15. Figure 2 indicates that the particle size of IOT was several times larger than that of GGBS. Under the appropriate mixing ratio, the pores formed by the IOT particles were effectively filled with GGBS particles. Furthermore, IOT contained a relatively high content of low-activity iron oxide, resulting in lower alkali activation activity. The addition of GGBS provided a significant amount of active silica and calcium, along with a highly polymerized glassy network structure [18,33].

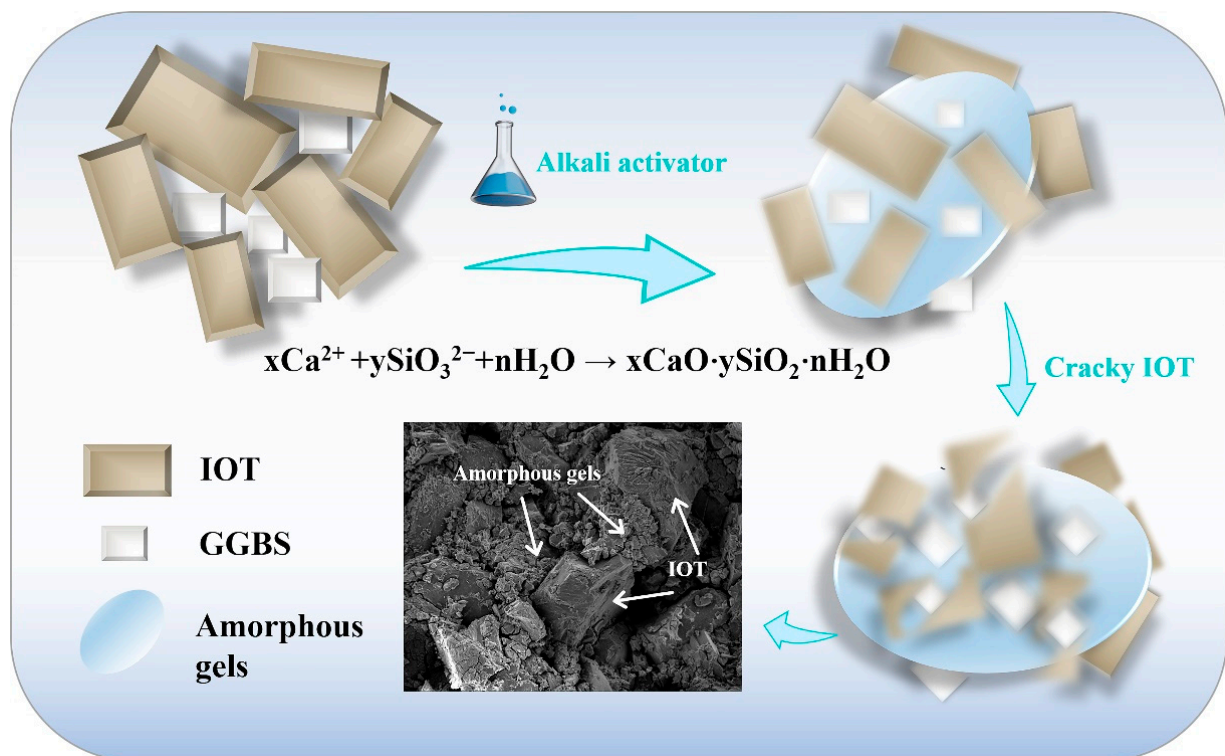


Figure 15. Reaction mechanism of alkali-activated IOT-GGBS mixtures.

Additionally, based on the XRD diffraction analysis results (Figure 11) and Table 2, both IOT and GGBS contained substantial amounts of calcium. Alkali metal ions were known to disrupt the weaker -O-Al-O- bonds in aluminosilicate glass structures and increase the non-bridging oxygen, leading to reduced polymerization and increased reactivity [36,37]. In the alkaline environment provided by the alkali activator, the soluble silica on the surfaces of GGBS and IOT particles underwent dissolution and acted as nucleation sites [46]. As shown in Figure 16, a substantial quantity of $[\text{OH}]^-$ could disrupt the Si-O-Al-O-Si and Si-O-Si bonds within the aluminosilicate glass network, initiating the depolymerization of the glass matrix into $[\text{SiO}_4]^{4-}$ and $[\text{AlO}_4]^{5-}$ tetrahedrons while releasing a large amount of Ca^{2+} ions. Subsequently, Ca^{2+} ions combined with the depolymerized $[\text{SiO}_4]^{4-}$ and $[\text{AlO}_4]^{5-}$ tetrahedrons, ultimately forming the essential C-S-H gels and C-A-H that contributed

significantly to the strength of the alkali-activated IOT bricks. As the reaction progressed further, IOT particles underwent fragmentation, leading to the formation of multiple smaller fragments. Consequently, the solution and small GGBS particles infiltrated the interior of the IOT particles, facilitating the continued generation of additional C-S-H gel. This phenomenon promoted enhanced interparticle bonding among the initially less reactive IOT particles, resulting in a further increase in the strength of the alkali-activated IOT bricks.

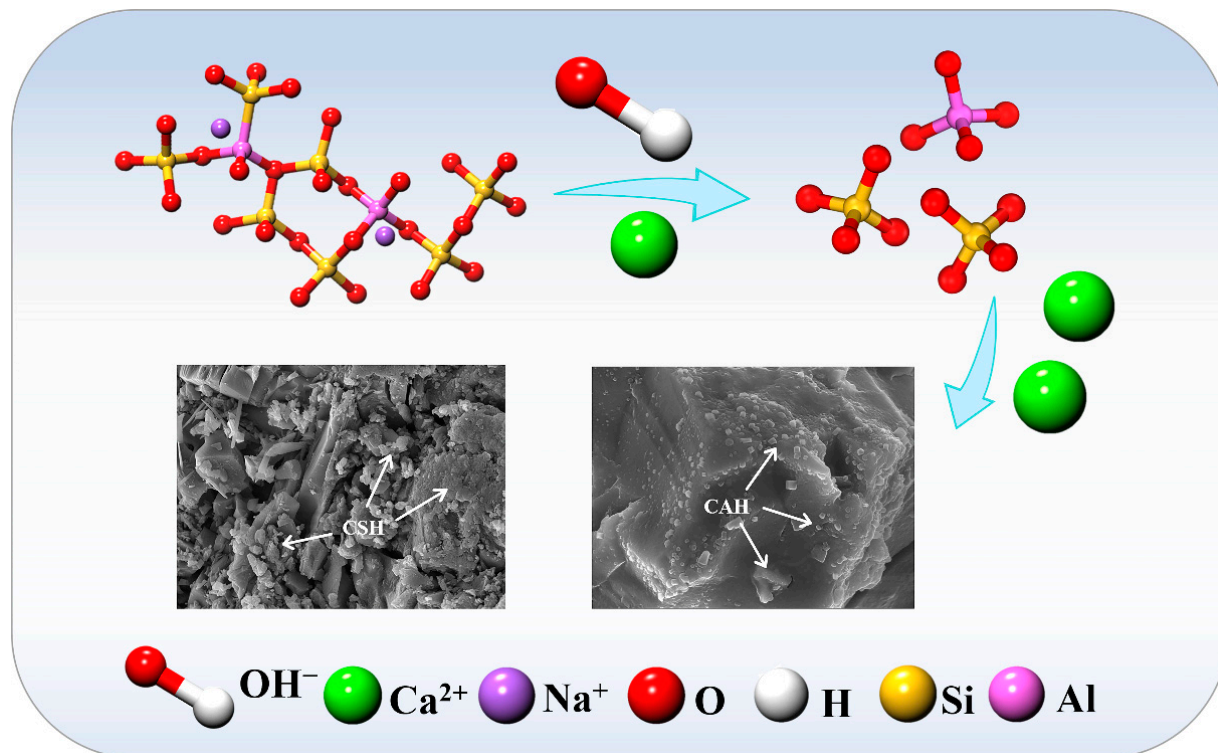


Figure 16. Depolymerization and polycondensation of aluminosilicates.

In summary, within the IOT-GGBS alkali-activated system, IOT primarily served as aggregates and participated partially in the reaction. Meanwhile, GGBS acted as the alkali-activated precursors, undergoing extensive reactions to produce C-S-H gel and C-A-H, thereby providing robust bonding within the system.

4. Conclusions

The production of alkali-activated high-content IOT bricks could be applied as a construction material in buildings, meeting the growing demand for construction materials while promoting ecological conservation and the advancement of a green economy. In this study, IOT was employed as the primary raw material, and a small proportion of GGBS was introduced as an auxiliary material, resulting in the successful synthesis of sustainable eco-friendly alkali-activated high-content IOT bricks. This study systematically investigated the effects of raw material mixing ratio, content, and modulus of alkali activator, molding pressure, and grain size distribution on the strength of alkali-activated bricks via compressive and flexural strength tests. Additionally, microstructural analyses using XRD, SEM, and FTIR were conducted to elucidate the alkali activation mechanism. The following conclusions were drawn from the research:

- (1) To fully utilize IOT and meet the Chinese JC/T422-2007 MU25 standard, a recommended IOT-to-GGBS ratio of 85:15 was proposed. At this ratio, the pores between the IOT particles were effectively filled with GGBS particles, resulting in bricks with a compressive strength of 31.72 MPa and a flexural strength of 2.83 MPa.

- (2) The strength of the bricks was enhanced by increasing the content of the alkali activator. When the content of the alkali activator reached 20%, the brick exhibited a compressive strength of 16.83 MPa and a flexural strength of 2.46 MPa. However, an excessively high modulus of the alkali activator led to the saturation of active Si, resulting in extensive encapsulation of particles by C-S-H gel and thus hindering the reaction. The optimal modulus of the alkali activator was determined to be 1.0 M, which yielded the highest compressive strength of 16.10 MPa and flexural strength of 2.13 MPa.
- (3) Using a molding pressure of 60 MPa, the brick achieved a compressive strength of 16.02 MPa and a flexural strength of 2.72 MPa. Elevating the molding pressure assisted in expelling air trapped within the pores, facilitating the infiltration of the alkali activator into the interior of the raw materials and enhancing the contact between particles.
- (4) Bricks prepared predominantly with fine-grained IOT exhibited a higher compressive strength compared to those dominated by coarse-grained IOT. The influence of the IOT grain size distribution on flexural strength was relatively minor, with fluctuations not exceeding 0.25 MPa.
- (5) For the IOT-GGBS alkali-activated system, IOT primarily functioned as aggregates and participated partially in the reaction, whereas GGBS served as the alkali-activated precursors, undergoing extensive reaction to produce C-S-H gel and C-A-H, thereby providing robust bonding within the system. Furthermore, an increase in the GGBS content might have led to the fragmentation of some IOT particles into smaller fragments, which then formed more stable aggregates under the influence of the C-S-H gel.

This study has several limitations and can provide information for future research. One limitation is that our research primarily focused on the effects of specific factors, such as raw material mixing ratios, alkali activator content, modulus, molding pressure, and grain size distribution. However, other parameters, such as curing conditions and environmental factors, can also influence the properties of bricks. Additionally, our study predominantly utilized local IOT resources, and the generalizability of our findings to other regions or materials should be approached with caution. Geographical variations in IOT properties may lead to different outcomes, and further studies should explore these regional disparities. Comparative studies involving IOT resources from different geographical locations could offer insights into the regional variations in IOT properties and their effects on brick production.

Author Contributions: Conceptualization, X.K. (Xin Kang); Methodology, X.K. (Xiangyang Kang), S.L. and X.K. (Xin Kang); Formal analysis, X.K. (Xiangyang Kang), Y.L., W.L., Y.Z. (Yuxian Zhou) and S.L.; Investigation, Y.L., W.L., Y.Z. (Yuxian Zhou), J.C., B.C., Y.Z. (Yong Zi) and J.F.; Resources, J.C., B.C., Y.Z. (Yong Zi) and J.F.; Data curation, Y.L., W.L., Y.Z. (Yuxian Zhou), J.C., B.C., Y.Z. (Yong Zi) and J.F.; Writing—original draft, S.L.; Writing—review & editing, Y.C. and X.K. (Xin Kang); Visualization, Y.C. and S.L.; Supervision, X.K. (Xin Kang); Funding acquisition, X.K. (Xiangyang Kang). All authors have read and agreed to the published version of the manuscript.

Funding: This research funded by the China Nuclear Industry Survey Design & Research Co., Ltd. (Grant No. 2022S04).

Data Availability Statement: No new data were created or analyzed in this study. Data sharing is not applicable to this article.

Acknowledgments: The authors are thankful to the reviewers for their constructive suggestions.

Conflicts of Interest: The authors declare no conflict of interest.

References

1. Anjum, F.; Naz, M.Y.; Ghaffar, A.; Kamran, K.; Shukrullah, S.; Ullah, S. Sustainable Insulating Porous Building Materials for Energy-Saving Perspective: Stones to Environmentally Friendly Bricks. *Constr. Build. Mater.* **2022**, *318*, 125930. [[CrossRef](#)]
2. Wang, S.; Gainey, L.; Mackinnon, I.D.; Allen, C.; Gu, Y.; Xi, Y. Thermal Behaviors of Clay Minerals as Key Components and Additives for Fired Brick Properties: A Review. *J. Build. Eng.* **2023**, *66*, 105802. [[CrossRef](#)]
3. Tanash, A.O.; Muthusamy, K.; Yahaya, F.M.; Ismail, M.A. Potential of Recycled Powder from Clay Brick, Sanitary Ware, and Concrete Waste as a Cement Substitute for Concrete: An Overview. *Constr. Build. Mater.* **2023**, *401*, 132760. [[CrossRef](#)]
4. Ahmari, S.; Zhang, L. Production of Eco-Friendly Bricks from Copper Mine Tailings through Geopolymerization. *Constr. Build. Mater.* **2012**, *29*, 323–331. [[CrossRef](#)]
5. Harech, M.; Labbilta, T.; Anasser, I.; El Hafiane, Y.; Abouliatim, Y.; Nibou, L.; Smith, A.; Mesnaoui, M. From by-Product to Sustainable Building Material: Reusing Phosphate Washing Sludge for Eco-Friendly Red Brick Production. *J. Build. Eng.* **2023**, *78*, 107575. [[CrossRef](#)]
6. Li, Y.; Ma, X.; Chen, Y.; Kang, X.; Yang, B. Superhydrophobicity Mechanism and Nanoscale Profiling of Pdms-Modified Kaolinite Nanolayers Via Ab Initio-Md Simulation and Atomic Force Microscopy Study. *Langmuir* **2023**, *39*, 8548–8558. [[CrossRef](#)]
7. Xin, Y.; Robert, D.; Mohajerani, A.; Tran, P.; Pramanik, B.K. Energy Efficiency of Waste Reformed Fired Clay Bricks-from Manufacturing to Post Application. *Energy* **2023**, *282*, 128755. [[CrossRef](#)]
8. Cheng, Y.; Huang, F.; Li, W.; Liu, R.; Li, G.; Wei, J. Test Research on the Effects of Mechanochemically Activated Iron Tailings on the Compressive Strength of Concrete. *Constr. Build. Mater.* **2016**, *118*, 164–170. [[CrossRef](#)]
9. Zhang, S.; Xue, X.; Liu, X.; Duan, P.; Yang, H.; Jiang, T.; Wang, D.; Liu, R. Current Situation and Comprehensive Utilization of Iron Ore Tailing Resources. *J. Min. Sci.* **2006**, *42*, 403–408. [[CrossRef](#)]
10. Wang, C.-L.; Ni, W.; Zhang, S.-Q.; Wang, S.; Gai, G.-S.; Wang, W.-K. Preparation and Properties of Autoclaved Aerated Concrete Using Coal Gangue and Iron Ore Tailings. *Constr. Build. Mater.* **2016**, *104*, 109–115. [[CrossRef](#)]
11. Chen, Z.; Chen, S.; Zhou, Y.; Zhang, C.; Meng, T.; Jiang, S.; Liu, L.; Hu, G. Effect of Incorporation of Rice Husk Ash and Iron Ore Tailings on Properties of Concrete. *Constr. Build. Mater.* **2022**, *238*, 127584. [[CrossRef](#)]
12. Zhang, N.; Tang, B.; Liu, X. Cementitious Activity of Iron Ore Tailing and Its Utilization in Cementitious Materials, Bricks and Concrete. *Constr. Build. Mater.* **2021**, *288*, 123022. [[CrossRef](#)]
13. Zhao, J.; Ni, K.; Su, Y.; Shi, Y. An Evaluation of Iron Ore Tailings Characteristics and Iron Ore Tailings Concrete Properties. *Constr. Build. Mater.* **2021**, *286*, 122968. [[CrossRef](#)]
14. Schoenberger, E. Environmentally Sustainable Mining: The Case of Tailings Storage Facilities. *Resour. Policy* **2016**, *49*, 119–128. [[CrossRef](#)]
15. Ma, X.-Y.; Kang, X.; Su, C.-X.; Chen, Y.-Q.; Sun, H.-M. Effects of Water Chemistry on Microfabric and Micromechanical Properties Evolution of Coastal Sediment: A Centrifugal Model Study. *Sci. Total Environ.* **2023**, *866*, 161343. [[CrossRef](#)]
16. Suzuki, Y.; Takenaka, C.; Tomioka, R.; Tsubota, H.; Takasaki, Y.; Umemura, T. Accumulation of Arsenic and Copper by Bryophytes Growing in an Aquatic Environment near Copper Mine Tailings. *Mine Water Environ.* **2016**, *35*, 265–272. [[CrossRef](#)]
17. Duan, P.; Yan, C.; Zhou, W.; Ren, D. Fresh Properties, Compressive Strength and Microstructure of Fly Ash Geopolymer Paste Blended with Iron Ore Tailing under Thermal Cycle. *Constr. Build. Mater.* **2016**, *118*, 76–88. [[CrossRef](#)]
18. Zhao, F.-Q.; Zhao, J.; Liu, H.-J. Autoclaved Brick from Low-Silicon Tailings. *Constr. Build. Mater.* **2009**, *23*, 538–541. [[CrossRef](#)]
19. Alves, P.; Dias, D.A.; Pontinha, A.D.R. Silica Aerogel-Rubber Composite: A Sustainable Alternative for Buildings' Thermal Insulation. *Molecules* **2022**, *27*, 7127. [[CrossRef](#)]
20. Almeida, V.O.; Silvestro, L.; Gleize, P.J.; Kirchheim, A.P.; Schneider, I.A. Schneider. Application of Leached Iron Ore Tailings to Produce Sustainable Cements. *Constr. Build. Mater.* **2023**, *377*, 131095. [[CrossRef](#)]
21. Huang, S.; Pi, Z.; Cai, C.; Li, H. Utilization of High-Sulfur Iron Ore Tailings in Cement Mortar by Considering the Influence of Curing Temperature and Tailing Content. *J. Build. Eng.* **2023**, *74*, 106826. [[CrossRef](#)]
22. Shettima, A.U.; Hussin, M.W.; Ahmad, Y.; Mirza, J. Evaluation of Iron Ore Tailings as Replacement for Fine Aggregate in Concrete. *Constr. Build. Mater.* **2016**, *120*, 72–79. [[CrossRef](#)]
23. Zhang, W.; Gu, X.; Qiu, J.; Liu, J.; Zhao, Y.; Li, X. Effects of Iron Ore Tailings on the Compressive Strength and Permeability of Ultra-High Performance Concrete. *Constr. Build. Mater.* **2020**, *260*, 119917. [[CrossRef](#)]
24. Fontes, W.C.; Mendes, J.C.; Da Silva, S.N.; Peixoto, R.A.F. Mortars for Laying and Coating Produced with Iron Ore Tailings from Tailing Dams. *Constr. Build. Mater.* **2016**, *112*, 988–995. [[CrossRef](#)]
25. Mendes, B.C.; Pedroti, L.G.; Fontes, M.; Ribeiro, J.C.L.; Vieira, C.M.F.; Pacheco, A.A.; de Azevedo, A.R. Technical and Environmental Assessment of the Incorporation of Iron Ore Tailings in Construction Clay Bricks. *Constr. Build. Mater.* **2019**, *227*, 116669. [[CrossRef](#)]
26. Chen, Y.; Zhang, Y.; Chen, T.; Zhao, Y.; Bao, S. Preparation of Eco-Friendly Construction Bricks from Hematite Tailings. *Constr. Build. Mater.* **2011**, *25*, 2107–2111. [[CrossRef](#)]
27. Yang, C.; Cui, C.; Qin, J.; Cui, X. Characteristics of the Fired Bricks with Low-Silicon Iron Tailings. *Constr. Build. Mater.* **2014**, *70*, 36–42. [[CrossRef](#)]
28. Luo, L.; Li, K.; Fu, W.; Liu, C.; Yang, S. Preparation, Characteristics and Mechanisms of the Composite Sintered Bricks Produced from Shale, Sewage Sludge, Coal Gangue Powder and Iron Ore Tailings. *Constr. Build. Mater.* **2020**, *232*, 117250. [[CrossRef](#)]

29. Zhao, Y.; Zhang, Y.; Chen, T.; Chen, Y.; Bao, S. Preparation of High Strength Autoclaved Bricks from Hematite Tailings. *Constr. Build. Mater.* **2012**, *28*, 450–455. [[CrossRef](#)]
30. Liu, J.; Ge, X.; Liu, P.; Song, G.; Hu, Z. Experimental Study on the Preparation of Cementitious Materials from Iron Ore Tailings by Activation. *Constr. Build. Mater.* **2023**, *385*, 131409. [[CrossRef](#)]
31. Thejas, H.K.; Hossiney, N. Alkali-Activated Bricks Made with Mining Waste Iron Ore Tailings. *Case Stud. Constr. Mater.* **2022**, *16*, e00973. [[CrossRef](#)]
32. Ali, H.A.; Sun, K.; Xuan, D.; Lu, J.-X.; Cyr, M.; Poon, C.S. Recycling of High-Volume Waste Glass Powder in Alkali-Activated Materials: An Efflorescence Mitigation Strategy. *J. Build. Eng.* **2023**, *65*, 105756. [[CrossRef](#)]
33. Gokul, V.; Steffi, D.A.; Kaviya, R.; Harni, C.; Dharani, S. Alkali Activation of Clayey Soil Using Ggbs and Naoh. *Mater. Today Proc.* **2021**, *43*, 1707–1713. [[CrossRef](#)]
34. Liu, G.; Rong, H.; Wang, J. Valorization of Converter Steel Slag in Sustainable Mortars by a Combined Alkali and Carbonation Activation. *J. Clean. Prod.* **2022**, *370*, 133519. [[CrossRef](#)]
35. Alam, S.; Das, S.K.; Rao, B.H. Strength and Durability Characteristic of Alkali Activated Ggbs Stabilized Red Mud as Geo-Material. *Constr. Build. Mater.* **2019**, *211*, 932–942. [[CrossRef](#)]
36. Lee, S.K.; Stebbins, J.F. Stebbins. Disorder and the Extent of Polymerization in Calcium Silicate and Aluminosilicate Glasses: O-17 Nmr Results and Quantum Chemical Molecular Orbital Calculations. *Geochim. Et Cosmochim. Acta* **2006**, *70*, 4275–4286. [[CrossRef](#)]
37. Stebbins, J.F.; Xu, Z. Nmr Evidence for Excess Non-Bridging Oxygen in an Aluminosilicate Glass. *Nature* **1997**, *390*, 60–62. [[CrossRef](#)]
38. Kang, X.; Zou, X.; Sun, H.-M.; Ma, X.-Y.; Chen, R.-P. Molecular Dynamics Simulations of Microstructure and Dynamic Shearing Behaviors of Kaolinite-Water-Salt System. *Appl. Clay Sci.* **2022**, *218*, 106414. [[CrossRef](#)]
39. Young, G.; Yang, M. Preparation and Characterization of Portland Cement Clinker from Iron Ore Tailings. *Constr. Build. Mater.* **2019**, *197*, 152–156. [[CrossRef](#)]
40. Li, L.; Zhang, H.; Guo, X.; Zhou, X.; Lu, L.; Chen, M.; Cheng, X. Pore Structure Evolution and Strength Development of Hardened Cement Paste with Super Low Water-to-Cement Ratios. *Constr. Build. Mater.* **2019**, *227*, 117108. [[CrossRef](#)]
41. Wang, W.; Gan, Y.; Kang, X. Synthesis and Characterization of Sustainable Eco-Friendly Unburned Bricks from Slate Tailings. *J. Mater. Res. Technol.* **2021**, *14*, 1697–1708. [[CrossRef](#)]
42. Zhang, Y.; Liu, B.; Gu, X.; Nehdi, M.L.; Zhang, L.V. Mechanochemical Activation of Iron Ore Tailing-Based Ternary Supplementary Cementitious Materials. *Constr. Build. Mater.* **2022**, *346*, 128420. [[CrossRef](#)]
43. Liu, M.; Yang, D.; Chen, L.; Chen, G.; Ma, Z. Effect of Silicate Modulus and Alkali Content on the Microstructure and Macroscopic Properties of Alkali-Activated Recycled Powder Mortar. *Constr. Build. Mater.* **2023**, *397*, 132365. [[CrossRef](#)]
44. Che, J.; Yang, R.; Wang, J.; Liu, H.; Hu, Y.; Doh, S.I. Research on Basic Mechanical Properties of Different Modulus Alkaline Excited Ecc. *Phys. Chem. Earth Parts A/B/C* **2022**, *128*, 103233. [[CrossRef](#)]
45. Wang, W.; Fan, C.; Wang, B.; Zhang, X.; Liu, Z. Workability, Rheology, and Geopolymerization of Fly Ash Geopolymer: Role of Alkali Content, Modulus, and Water–Binder Ratio. *Constr. Build. Mater.* **2023**, *367*, 130357. [[CrossRef](#)]
46. Sun, B.; Sun, Y.; Ye, G.; De Schutter, G. A Mix Design Methodology of Slag and Fly Ash-Based Alkali-Activated Paste. *Cem. Concr. Compos.* **2022**, *126*, 104368. [[CrossRef](#)]
47. Xia, D.; Chen, R.; Cheng, J.; Tang, Y.; Xiao, C.; Li, Z. Desert Sand-High Calcium Fly Ash-Based Alkali-Activated Mortar: Flowability, Mechanical Properties, and Microscopic Analysis. *Constr. Build. Mater.* **2023**, *398*, 131729. [[CrossRef](#)]
48. Prasanphan, S.; Wannagon, A.; Kobayashi, T.; Jiemsirilers, S. Reaction Mechanisms of Calcined Kaolin Processing Waste-Based Geopolymers in the Presence of Low Alkali Activator Solution. *Constr. Build. Mater.* **2019**, *221*, 409–420. [[CrossRef](#)]
49. Ranjbar, N.; Mehrali, M.; Maheri, M.R.; Mehrali, M. Hot-Pressed Geopolymer. *Cem. Concr. Res.* **2017**, *100*, 14–22. [[CrossRef](#)]
50. Bayrak, B.; Öz, A.; Benli, A.; Kavaz, E.; Kaplan, G.; Aydın, A.C. Physico-Mechanical and Shielding Properties of Alkali-Activated Slag Composites Incorporating Cement Clinker Aggregate: Effect of High Temperature and Particle Size. *J. Build. Eng.* **2023**, *67*, 105982. [[CrossRef](#)]
51. Kang, X.; Gan, Y.; Chen, R.; Zhang, C. Sustainable Eco-Friendly Bricks from Slate Tailings through Geopolymerization: Synthesis and Characterization Analysis. *Constr. Build. Mater.* **2021**, *278*, 122337. [[CrossRef](#)]
52. Labò, S.; Marini, A. In-Plane Flexural Behavior of Hollow Brick Masonry Walls with Horizontal Holes. *Eng. Struct.* **2022**, *273*, 115086. [[CrossRef](#)]
53. Miah, J.; Babafemi, A.J.; Paul, S.C.; Kong, S.Y.; Li, Y.; Jang, J.G. Eco-Friendly Concrete with Chemically Treated End-of-Life Tires: Mechanical Strength, Shrinkage, and Flexural Performance of Rc Beams. *Constr. Build. Mater.* **2022**, *351*, 128970. [[CrossRef](#)]
54. He, P.; Zhang, B.; Lu, J.-X.; Poon, C.S. Reaction Mechanisms of Alkali-Activated Glass Powder-Ggbs-Cac Composites. *Cem. Concr. Compos.* **2021**, *122*, 104143. [[CrossRef](#)]
55. Ahmari, S.; Zhang, L. Utilization of Cement Kiln Dust (Ckd) to Enhance Mine Tailings-Based Geopolymer Bricks. *Constr. Build. Mater.* **2013**, *40*, 1002–1011. [[CrossRef](#)]
56. Amin, N.U.; Faisal, M.; Muhammad, K.; Gul, S. Synthesis and Characterization of Geopolymer from Bagasse Bottom Ash, Waste of Sugar Industries and Naturally Available China Clay. *J. Clean. Prod.* **2016**, *129*, 491–495. [[CrossRef](#)]
57. Novais, R.M.; Ascensão, G.; Tobaldi, D.M.; Seabra, M.P.; Labrincha, J.A. Biomass Fly Ash Geopolymer Monoliths for Effective Methylene Blue Removal from Wastewaters. *J. Clean. Prod.* **2018**, *171*, 783–794. [[CrossRef](#)]

58. Huseien, G.F.; Hamzah, H.K.; Sam, A.R.M.; Khalid, N.H.A.; Shah, K.W.; Deogrescu, D.P.; Mirza, J. Alkali-Activated Mortars Blended with Glass Bottle Waste Nano Powder: Environmental Benefit and Sustainability. *J. Clean. Prod.* **2020**, *243*, 118636. [[CrossRef](#)]
59. Puertas, F.; Torres-Carrasco, M. Use of Glass Waste as an Activator in the Preparation of Alkali-Activated Slag. Mechanical Strength and Paste Characterisation. *Cem. Concr. Res.* **2014**, *57*, 95–104. [[CrossRef](#)]

Disclaimer/Publisher's Note: The statements, opinions and data contained in all publications are solely those of the individual author(s) and contributor(s) and not of MDPI and/or the editor(s). MDPI and/or the editor(s) disclaim responsibility for any injury to people or property resulting from any ideas, methods, instructions or products referred to in the content.